RSC Advances

ROYAL SOCIETY OF CHEMISTRY

www.rsc.org/advances

RSC Advances

RSCPublishing

ARTICLE

One-step synthesis of the nickel foam supported network-like ZnO nanoarchitectures assembled with ultrathin mesoporous nanosheets with improved lithium storage performance

Cite this: DOI: 10.1039/x0xx00000x

Received 00th January 2012,
Accepted 00th January 2012

DOI: 10.1039/x0xx00000x

www.rsc.org/

Xiaoyu Wu, Songmei Li*, Bo Wang, Jianhua Liu, Mei Yu

A novel network-like ZnO nanoarchitecture supported on nickel foam (ZnO@NF) is synthesized successfully via a facile one-step hydrothermal route. The obtained ZnO nanoarchitectures firmly grow on the skeleton of nickel foam, exhibiting network-like porous structures assembled with massive interconnected ultrathin mesoporous ZnO nanosheets. When evaluated directly as binder-free anode for lithium-ion batteries, the resultant ZnO@NF electrodes exhibit excellent lithium storage performance with a high reversible capacity (760.5 mAh g^{-1} at a current density of 200 mA g^{-1}), improved cycling performance (the capacity maintains at 534.3 mAh g^{-1} after 100 cycles), and better rate capability compared with binder-containing counterparts. The improved electrochemical performances could be attributed to the unique network-like mesoporous microstructure and the integrated smart architecture, which could facilitate the electron transport and lithium ion diffusion, and buffer the volume change during repeated charge/discharge process effectively.

Introduction

Nowadays, the demand for sustainable and clean energy is becoming more and more critical owing to the emergence of applications such as electric vehicles (EVs), hybrid electric vehicles (HEVs) and the various portable electronic devices currently available.[1] Lithium-ion batteries (LIBs) have drawn world-wide interest due to their high energy density, long cycle life, design flexibility and environmental benignity.[2-4] In order to meet the ever-growing demand for future portable and flexible LIBs with high energy and high power, developing alternative electrode materials with high-performance, flexibility and lightweight becomes greatly desired.[5] Electrochemical active transition-metal oxides (TMOs), such as Co_3O_4, MnO_2, SnO_2 Fe_2O_3 and ZnO, have been widely investigated as anode materials to replace conventional commercial graphite because of their high theoretical capacities, low cost, and environmental friendliness.[6-11]

Zinc oxide (ZnO), as an important member of TMOs, has the advantages of chemical stability, low cost, easy to prepare, eco-friendly nature, and possessing a high theoretical capacity of 987 mAh g^{-1} based on alloying reaction and conversion reaction mechanism when used as LIBs anodes.[11-13] However, due to low electronic conductivity and large volume change during charge/discharge process, ZnO-based anodes still suffer from poor cycling stability and low reversible capacity.[14,15] Therefore, numerous efforts have been devoted to overcoming these problems, mainly including two solutions: (1) doping with other better conductors such as Ni, Co and C to improve the conductivity;[16-20] (2) designing mesoporous nanostructured materials to buffer the volume changes during the charge/discharge process, increase the electrode/electrolyte contact areas, shorten the diffusion distances of Li^+, and eventually improve the lithium storage performance of ZnO-based anodes.[13,21,22] Nonetheless, the ZnO-based anode usually delivers a reversible capacity below 500 mAh g^{-1}, which is far less than its theoretical value, and its cycling stability and high rate capability still could not satisfy the practical applications.[15] Therefore, rational morphology and structure design of ZnO-based anode for the performance improvement still remains a significant challenge.

Recently, fabricating integrated binder-free electrodes by directly coating active materials on self-supported three-dimensional (3D) porous conducting substrate have emerged as a new direction. The integrated binder-free electrodes can avoid

*Key Laboratory of Aerospace Advanced Materials and Performance of Ministry of Education, School of Materials Science and Engineering, Beihang University, Beijing, 100191, China. E-mail: songmei_li@buaa.edu.cn; Fax: +86-10-82317103; Tel: +86-10-82317103

† Electronic supplementary information (ESI) available. See DOI:

the use of any binder or conductive additives, offer a larger electrode/electrolyte contact area, and provide 3D interconnected network of both electron and ion pathways, allowing for efficient charge and mass exchange during redox reactions.[23,24] Among the various 3D porous conducting substrates, nickel foam (NF) is considered to be one of the most attractive current collector to support electrochemical active materials because of its high electric conductivity, low cost, and good mechanical stability.[25-27]

Based on the above considerations, a novel network-like porous ZnO nanoarchitecture supported on nickel foam (ZnO@NF) was synthesized successfully via a facile hydrothermal route, which is directly used as binder-free electrodes for electrochemical evaluation. Different from the traditional synthesis methods of ZnO-based nanoarchitectures, this method is a facile one-step procedure avoiding the subsequent thermal annealing at high temperature.[11,18,20,22] The obtained ZnO nanoarchitectures firmly attached to the skeleton of nickel foam, exhibiting network-like structures assembled by massive interconnected ultrathin mesoporous nanosheets. Benefiting from the unique network-like mesoporous microstructures and the integrated smart architectures, the ZnO@NF electrodes exhibit enhanced lithium storage performance as binder-free anodes for LIBs compared to the binder-containing counterparts.

Experimental

Chemicals

All reagents used in the experiment were of analytical purity grade and used as received without further purification. Typically, zinc nitrate hexahydrate ($Zn(NO_3)_2\ 6H_2O$), hexamethylenetetramine (HMTA), ammonia ($NH_3\cdot H_2O$, 25 wt.%) are purchased from Beijing chemical Co., Ltd. (Beijing, China). Nickel foams are purchased from Lyrun Co., Ltd. (Changsha, China).

Synthesis of the ZnO@NF composites

The network-like ZnO nanoarchitectures were grown directly on nickel foams via a hydrothermal route. In detail, prior to hydrothermal reaction, nickel foam cut into piece of 3 cm ×4 cm in size was degreased with acetone for 10 min, etched with 1M HCl solution for 10 min, and then washed by deionized water and ethanol with sonication for 10 min, respectively. At the same time, 4.46 g of $Zn(NO_3)_2\ 6H_2O$, 2.10 g of HMTA and 2 mL of ammonia were dissolved in 70 mL distilled water under constant magnetic stirring for 30 min. Then the obtained homogeneous solution was transferred into the 100 mL polytetrafluoroethylene (PTFE) Teflon-lined stainless steel autoclave with the nickel foam immersed into the reaction solution with a 45° angle and keeping sealed at 90 ℃ for 6 h. After the hydrothermal reaction, the nickel foam coated with white product was washed by deionized water and ethanol for several times, and the ZnO@NF composites as final products were obtained after natural drying. For comparison, ZnO nanosheets powders were prepared in the same reaction system without the addition of nickel foam substrates.

Materials Characterization

The crystallographic structures of the products were characterized by a powder X-ray diffraction system (XRD, Rigaku D/max-2200PC) equipped with Cu Kα radiation (λ=0.15418 nm), with the diffraction angle in the range of 20-80°. The morphology and microstructure of the products were characterized by field-emission scanning electron microscope (FE-SEM, JEOL JSM-7500F) and transmission electron microscope (TEM, JEOL JEM-2100F). The elemental compositions of the products were analyzed by energy-dispersive X-ray spectroscope (EDS) equipped to FE-SEM. The N_2 adsorption/desorption were determined by Brunauer-Emmett-Teller (BET) measurements using an ASAP-2010 surface area analyzer.

Electrochemical measurements

Electrochemical measurements were performed at room temperature on 2025 coin-type cells assembled in an argon-filled glove box, in which oxygen and water contents were less than 1 ppm. The as-prepared ZnO@NF composites were punched in the form of 12 mm diameter disks, and then used as the working electrode directly without any conductive additive and polymer binder. Nickel foams without the loading of ZnO were also punched in the form of 12mm diameter disks. In order to reduce the mass uncertainty of the electrodes, 10 pieces of the samples (nickel foams and ZnO@NF composites, respectively) were weighed together. Calculated by the weight of the total mass, the mass loading of the active materials (ZnO) for the testing electrodes was about 2.0 mg cm^{-2}. While the ZnO mass loading of the specific electrodes used to calculate the specific capacities of the composites was calculated by weighing the nickel foam disks before and after the loading of ZnO for several times. For comparison, the as-prepared ZnO nanosheets powders were also used as active materials to form working electrodes. The corresponding pasted electrodes were prepared by coating a N-methylpyrrolidinone (NMP) slurry composed of 80 wt.% active materials, 10 wt.% polyvinylidene fluoride (PVDF) and 10 wt.% acetylene black on steel foil, followed by drying at 40℃ in vacuum oven for 12 h. A metallic lithium foil served as both the counter electrode and the reference electrode, a polypropylene (PP) microporous film (Celgard 2400) was used as separator, and a solution of 1 M $LiPF_6$ dissolved in a 1:1 (v/v) mixture of ethylene carbonate (EC) and dimethyl carbonate (DMC) was used as electrolyte. The cyclic voltammetry (CV) and galvanostatic charge-discharge tests were conducted on LAND CT2001A battery-testing instrument and multichannel Arbin BT2000 system in the potential range of 0.005-3.0 V (vs. Li^+/Li) at room temperature. Electrochemical impedance spectroscopy (EIS) measurements were performed using an electrochemistry system (PARSTAT 2273, Princeton Applied Research, USA) by applying an AC voltage amplitude of 5 mV in the frequency range from 100 kHz to 100 mHz.

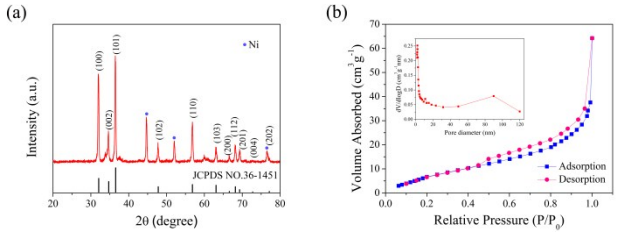

Fig. 1 (a) XRD pattern of the as-prepared ZnO@NF composites, and the standard XRD pattern of hexagonal ZnO. (b) N_2 adsorption/desorption isotherm, and the insert corresponding pore size distribution of ZnO nanoarchitectures.

Results and discussion

The phase structures of the as-prepared products were analyzed by a powder X-ray diffraction system. Fig. 1(a) shows the XRD pattern of the ZnO@NF composites and the standard XRD pattern of hexagonal phase of wurtzite-type ZnO. Besides three strong peaks from the nickel foam substrate, the typical diffraction peaks of the samples could be well indexed to crystal planes of the well-crystallized ZnO phase with hexagonal wurtzite structure, which is in agreement with the standard XRD pattern of hexagonal ZnO (JCPDS card no.36-1451), indicating that the crystalline ZnO has been formed after hydrothermal reaction.[15,21,28] No obvious diffraction peaks of impurities were detected, indicating the good crystallinity and purity of the as-prepared ZnO products grown on nickel foam. Moreover, all the diffraction peaks of the as-prepared powders are also well matched with the standard pattern of hexagonal ZnO (Fig. S1, Supporting Information), confirming the composition of the powders.

Full nitrogen adsorption/desorption isotherm was collected to calculate the pore size distribution and specific surface area of the ZnO nanoarchitectures scratched from the nickel foam. As shown in Fig. 1(b), the isotherm shows a type IV curve with a distinct H3-type hysteresis loop in the relative pressure range of 0.45-1.0 P/P_0, which is ascribed to the presence of mesoporous structures in the nanoarchitectures.[29,30] According to the Brunauer-Emmett-Teller (BET) method, the specific surface area of the sample is calculated to be 48.06 m^2 g^{-1}. Meanwhile, the Barrett-Joyner-Halenda (BJH) pore size distribution further confirms the mesoporous and macropores feature of the obtained ZnO nanoarchitectures. As shown in the insert of Fig. 1(b), a sharp peak at the pore size range of 2-5 nm can be seen clearly, which is attributed to the mesoporous channels in ZnO nanoarchitectures, while the sharp peak at ~ 90 nm corresponds to macropores. Such a high specific surface area of the ZnO nanoarchitectures with massive mesopores and macropores can facilitate the transport of electrons and ions efficiently and buffer the volume change during charge/discharge process to improve the cycling stability, thus improving lithium storage performance of the electrode materials.[29,31-33]

The morphology and microstructure of the as-prepared ZnO@NF composites were investigated by FE-SEM and TEM. The optical image of the pristine nickel foam and the ZnO@NF composites is shown in Fig. 2(a). The obvious color change and the final uniform color of the nickel foam indicate the uniform coating of active materials. The nickel foam substrate shows a three-dimensional (3D) porous structure, which is further confirmed by the SEM image shown in Fig. S2 (Supporting Information). Fig. 2(b-e) are the typical SEM images of the as-prepared ZnO@NF composites with different magnification. As shown in Fig. 2(b), the ZnO nanoarchitectures are grown upon the whole 3D nickel skeleton completely without spalling. It can be seen clearly that the surface of the nickel foam after hydrothermal reaction becomes rough compared to the smooth surface of the pristine nickel foam (Fig. S2, Supporting Information). From the magnified SEM images of Fig. 2 (c-e), it can be seen that the ZnO nanoarchitectures supported on nickel foam exhibit unique network-like structures, which are assembled by massive interconnected ultrathin nanosheets. As shown in Fig. 2(d,e), the building block nanosheets are curved with large lateral sizes of ~400 nm, and randomly connected with the adjacent nanosheets to assemble into continuous and interconnected porous architectures, thereby forming a large number of voids and electroactive sites.[23] Besides, the building block nanosheets show the morphologies of bending, curling, and crumpling, which is due to the much larger lateral size than the thickness. Such unique microstructure is of great significance for lithium storage, not only providing stable structure for the electrodes, but also facilitating the electron transfer and ion diffusion.[23,34] In addition, as shown in Fig. S3 (Supporting Information), without the supporting of nickel foam, the as-prepared ZnO powders exhibit the morphology of disorderly stacked nanosheets with severe aggregation, which

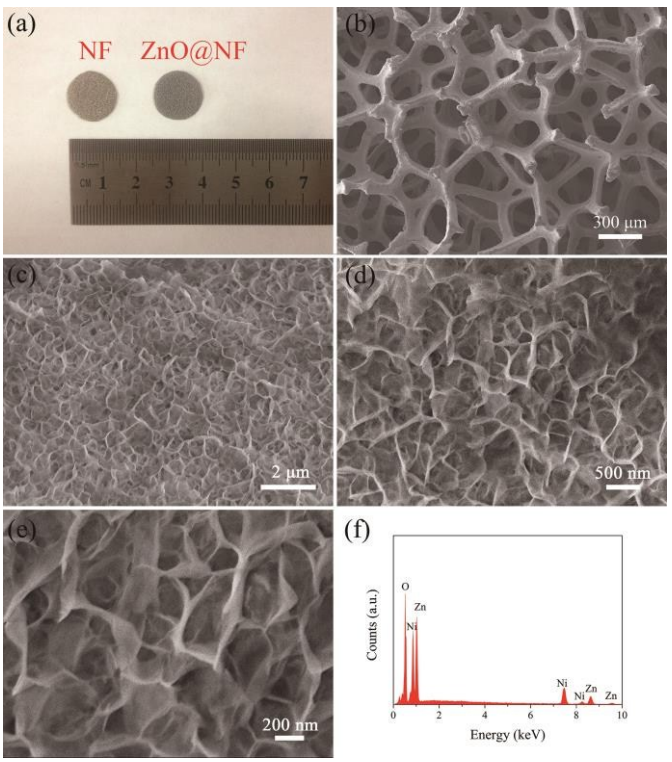

Fig. 2 (a) Optical image of nickel foam and as-prepared ZnO@NF composites. (b-e) Typical SEM images of the ZnO@NF composites at different magnifications. (f) EDS spectrum of the ZnO@NF composites.

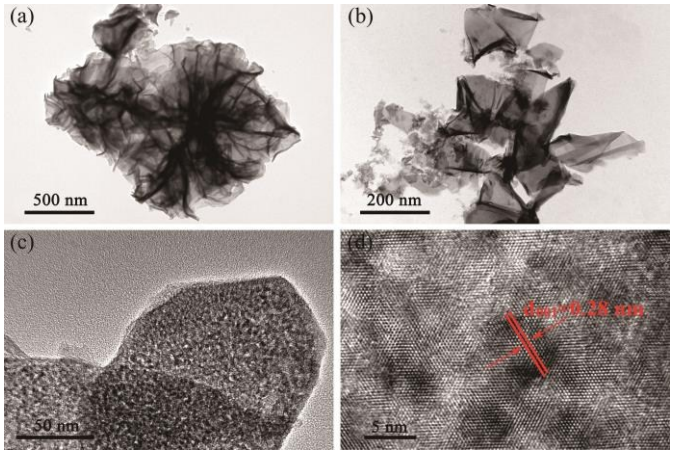

Fig. 3 (a, b, c) TEM images the ZnO nanosheets in ZnO@NF composites at different magnifications; (d) HRTEM image of the ZnO nanosheets in ZnO@NF composites.

are much thicker than the building block nanosheets of the ZnO@NF composites. Moreover, the element composition of the composites was confirmed by EDS analysis. According to the EDS spectrum in Fig. 2(f), the ZnO@NF composites are mainly composed of Ni，Zn and O elements, consisting with the XRD results.

In order to further confirm the microstructures of the as-prepared ZnO@NF composites, TEM images of the composites were obtained and shown in Fig. 3. Note that the samples for TEM measurements were prepared as follows: the ZnO@NF composites were ultrasonically dispersed in ethanol for 60 min, and the detached ZnO nanoarchitectures from NF were dropped onto a 200-mesh TEM grid, followed by drying under ambient conditions. As seen in Fig. 3(a), the low magnification TEM image confirm the interconnected network-like nanostructures of the products built up of flexible and ultrathin nanosheets, which is in good agreement with the SEM results. And the TEM image of the scattered nanosheets in Fig. 3(b) shows the obvious intrinsic wrinkles or corrugations of the ultrathin nanosheets. Moreover, as shown in the magnified TEM images of Fig. 3(c), a large number of mesopores (about 2-5 nm) are uniformly distributed on the nanosheets, further suggesting the ultrathin and mesoporous structure of the building block nanosheets. In addition, the high-resolution TEM (HRTEM) image in Fig. 3(d) reveals the lattice fringes with lattice spacings of 0.28 nm, which agrees well with the (100) crystal planes of hexagonal phase ZnO, consisting with the XRD results.[11]

The ZnO@NF composites exhibit remarkable electrochemical performances when used directly as anodes for LIBs without binder or conductive additives, as shown in Fig. 4. As mentioned above, the electrochemical performances of traditional slurry-coating electrodes of ZnO powders coated on steel foils were evaluated as a control experiment for comparison, in which the ZnO powders were mixed with the conductive carbon black and polyvinylidene fluoride (PVDF) binder in a weight ratio of approximately 8:1:1. Cyclic voltammetry (CV) measurements were conducted to identify the electrochemical reactions occurred during the lithiation/delithiation process of the electrodes. Fig. 4(a) shows the initial there cyclic voltammetry (CV) curves of the ZnO@NF electrodes at a scan rate of 0.1 mV s^{-1} between 0.005 and 3.0 V (vs. Li^+/Li). In the first cathodic scan, an intense peak and two weak peaks are observed at 0.20, 0.67 and 0.92 V respectively, which can be assigned to the first electrochemical process of the ZnO materials, including the reduction of ZnO to Zn, the formation of Li-Zn alloy, as well as the decomposition of organic electrolyte to form a solid electrolyte interphase (SEI) layer at the electrode-electrolyte interface.[13,19,21] In the first anodic scan, the three peaks located at 0.34, 0.55 and 0.69V, as well as a broad peak located at ~1.38V, are ascribed to the multi-step dealloying process of Li-Zn alloy. And the peak at ~2.64V corresponds to the convention reaction of Zn to ZnO.[13,35] In the second and following cycles, two cathodic peaks are observed at 0.31V and 0.68 V, corresponding to the alloying process. Obviously, the CV curves of the second and following cycles are different from that of the first cycle, while the second and following CV curves are almost overlapped, presenting excellent reversible performances except for the irreversible reactivity in the first cycle. Therefore, on the basis of above analysis, the electrochemical reactions of the ZnO@NF electrodes can be described as follows:[13,19, 35,36]

In the first discharge process:

$$ZnO + 2Li \rightarrow Zn + Li_2O \quad (1)$$

$$Zn + Li \rightarrow LiZn \quad (2)$$

In the following charge/discharge processes:

$$LiZn \leftrightarrow Li + Zn \quad (3)$$

$$Zn + Li_2O \leftrightarrow ZnO + 2Li \quad (4)$$

In fact, the 3D nickel foam skeleton plays a key role in their reversible performances, which supports the network-like ZnO nanoarchitectures with excellent structure stabilities, thereby maintaining their high specific surface areas and short diffusion distances effectively.[25,27]

The electrochemical performance of the electrodes have been further examined by galvanostatic charge-discharge tests at a current density of 200 mA g^{-1} in the potential range of 0.005-3.0 V (vs. Li^+/Li). As mentioned above, the ZnO mass loading of the specific electrodes used to calculate the electrochemical performance of the composites is calculated by weighing the nickel foam disks before and after the loading of ZnO for several times. Fig. 4(b) shows the charge-discharge profiles of the ZnO@NF electrode in the 1^{st}, 2^{nd}, 3^{rd}, 50^{th} and 100^{th} cycles. The initial discharge and charge capacities of the electrode are 1142.8 and 758.8 mAh g^{-1}, respectively, corresponding to an initial Coulombic efficiency of 66.4%. The initial capacity loss of the electrode can be mainly ascribed to the incomplete decomposition of Li_2O and the difficult dissolution of the SEI layers, as well as the irreversible lithium loss.[37-39] Meanwhile, compared to the theoretical capacity (978 mAh g^{-1}) of ZnO, the extra capacity at the first discharge may resulted from the formation of SEI layers on the electrode/electrolyte interface.[13,38-41] In the second cycle, the discharge and charge capacities of the ZnO@NF electrodes are 760.5 and 751.4 mAh g^{-1} respectively, and the Coulombic

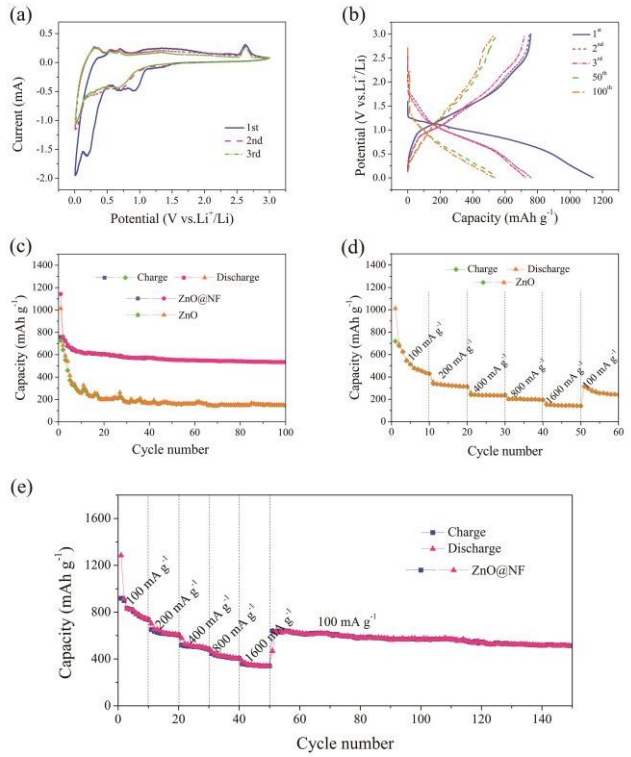

Fig. 4 (a) Cyclic voltammograms of the ZnO@NF electrodes for the initial three cycles at a scan rate of 0.1 mV s^{-1} in the voltage range of 0.005-3.0 V; (b) Charge-discharge voltage profiles of the ZnO@NF electrodes at a current density of 200 mA g^{-1}; (c) Comparison of cycling performance of the ZnO@NF electrodes and ZnO powders pasted electrodes at a current density of 200 mA g^{-1}; Rate capability of (d) the ZnO powders pasted electrodes and (f) the ZnO@NF electrodes.

efficiency rapidly rises to 98.8% and then increase gradually to nearly 100% in the subsequent cycles. The cycling performance curves of the two electrodes are shown in Fig. 4(c), which were tested at a current density of 200 mA g^{-1} for 100 cycles in the voltage range of 0.005-3.0 V (vs. Li^+/Li), indicating the excellent cycling stability of the ZnO@NF electrodes. As shown in Fig. 4(c), the discharge capacities of the ZnO@NF electrodes decrease gradually in the first 10 cycles, and then maintain at about 600mAh g^{-1} with no significant fading. After 100 cycles, the reversible capacity of ZnO@NF electrodes maintains as high as 534.3 mAh g^{-1}, corresponding to 70.4% of the discharge capacity of the second cycle. In comparison, the ZnO powders pasted electrodes exhibiting worse cycling stability, which the capacities drop sharply to ~200 mAh g^{-1} in the first 20 cycles. Besides, the cycling stability of ZnO@NF electrodes are outstanding compared to that of ZnO-based anodes reported in the previous literatures: such as the mesoporous ZnO nanosheets (the capacity is maintained at 420 mAh g^{-1} after 50 cycles at the current density of 100 mA g^{-1}),[41] the porous ZnO nanosheets (the capacities maintain at about 400 mAh g^{-1} after 100 cycles at the current density of 500 mA g^{-1}),[13] and ZnO nanorod arrays (keep a capacity of ~310 mAh g^{-1} after 40 cycles at 0.1 mA cm^{-1}).[21] In addition, as shown in Fig. 4(c), the ZnO@NF electrodes exhibit much higher capacities than the ZnO powders pasted electrodes, especially after several charge/discharge cycles, further indicating the superiority of the ZnO@NF composites.

Furthermore, the rate capability of the ZnO@NF and ZnO powders pasted electrodes was investigated, in which the electrodes were cycled at various current densities ranging from 100 to 1600 mA g^{-1}, and finally returned to 100 mA g^{-1}. As shown in Fig. 4(e), the average discharge capacities of the ZnO@NF electrodes at different current densitiies of 100, 200, 400 and 800 mA g^{-1} are 847.7, 633.4, 513.9 and 424.4 mAh g^{-1}, respectively. Even at a high current density of 1600 mA g^{-1}, a favorable specific capacity of ~350 mAh g^{-1} can be maintained, which is much higher than those of the ZnO powders pasted electrodes (~140 mAh g^{-1}) as shown in Fig. 4(d). Besides, after deep cycling at the high current density of 1600 mA g^{-1}, the specific capacities of ZnO@NF electrodes are nearly recovered to its initial values when the current density returned back 100 mAg^{-1} after 50 cycles, indicating their good reversibility and excellent cycling stability. Therefore, the ZnO powders pasted electrodes exhibit much lower capacities and possess worse rate capability as a result of sluggish ionic adsorption/diffusion kinetics and poor electronic conductivity. More importantly, when charged and discharged continuously at a current density of 100 mAh g^{-1} after the rate capability measurement, the ZnO@NF electrodes maintain a stable high capacity much more than 500 mAh g^{-1}, even after 150 cycles, further indicating their excellent cycling stability. In addition, the morphology and structure of the network-like ZnO retain almost intact after 100 cycles (Fig. S4, Supporting Information), which demonstrate the structural stability of as-obtained ZnO nanoarchitectures and the strong adhension of ZnO on the nickel foam.

Additionally, EIS measurements were performed on the electrodes to further clarify the improved lithium storage performance of the ZnO@NF electrodes. Fig. 5(a) compares the Nyquist plots of the ZnO@NF and ZnO powders pasted electrodes in the frequency range from 100 kHz to 100 mHz. Obviously, the Nyquist plots are composed of a semicircle in the high-middle frequency region and a slope line in the low frequency region. The semicircle in high-frequency region is attributed to the formation of the SEI layer and contacting impedance between active materials and electrolyte, the semicircle in the middle frequency range can be assigned to the charge-transfer resistance (R_{ct}) of electrode/electrolyte interface.[19,42-44] From Fig. 5(a), it can be seen clearly that the diameter of the semicircle for ZnO@NF electrode in high-middle frequency region is much smaller than that of the ZnO powders pasted electrode, indicating that the ZnO@NF electrodes possess the lower contact and electron-transfer resistances. Furthermore, the slopping line presented in the low-frequency region of the Nyquist plots suggests that the diffusion of Li^+ is the rate-determining step. The diffusion coefficient of Li^+ can be calculated as follows:[44-46]

$$D_{Li^+} = R^2T^2/(2A^2n^4F^4C^2\sigma_w^2) \quad (5)$$

where D_{Li^+} is the diffusion coefficient, R is the gas constant, T is the absolute temperature, n is the reacting electron number per molecule, A is the area surface of the electrode, F is the

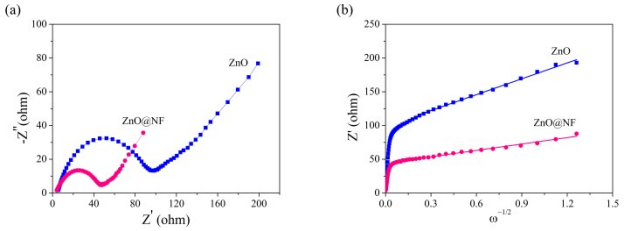

Fig. 5 (a) Nyquist plots, (b) Randles plots of the ZnO@NF electrodes and ZnO powders pasted electrodes.

Faraday constant, C is the molar concentration of Li^+, and σ_w is the Warburg coefficient. According to the semi-infinite diffusion model, the Warburg impedance (Zw) in anodes is formulated according to the following equation:[44]

$$Z_w = \sigma_w \omega^{-1/2}(1\text{-}j) \quad (6)$$

where ω is the angular frequency. According to equation (6), the Warburg coefficient (σ_w) can be calculated based on the relationship between Z_w and $\omega^{-1/2}$. Therefore, the plot of the Z_w versus $\omega^{-1/2}$ ("Randles plot") for the electrodes was built, as shown in Fig. 5(b), where the slope of the fitted line in low-frequency region is the Warburg coefficient (σ_w). Obviously, for ZnO@NF electrodes, the value of σ_w is smaller than that of ZnO powders pasted electrodes, thereby possessing higher Li^+ diffusion coefficient (D_{Li^+}). It is observed that the Warburg coefficients (σ_w) of ZnO and ZnO@NF are 78.59 and 31.60, respectively. By combining the equations (5), the lithium diffusion coefficient of ZnO and ZnO@NF are calculated to be 7.03×10^{-14} cm^2 s^{-1} and 4.35×10^{-13} cm^2 s^{-1}, respectively. Theoretically, the enhancement of Li^+ diffusivity for ZnO@NF may be attributed to that the 3D nickel foam supported structure is beneficial for the better wetting of the active material with the electrolyte, thus facilitating the faster Li^+ transport across the electrode/electrolyte interface.[25,27] On the other hand, the network-like porous nanoarchitecture can ensure electroactive materials in high contact with electrolyte and are more favorable for rapid Li^+ diffusion than the disorderly stacked ZnO nanosheets.[47]

Based on the analyses above, the ZnO@NF composites exhibit enhanced lithium storage performances, which is believed to result from the rationally designed nanostructure and the integrated smart architecture.[23] Firstly, compared with the traditional binder-containing pasted electrode, directly growing interconnected network-like ZnO nanoarchitectures on the skeleton of nickel foam with robust mechanical adhesion not only simplifies the electrode processing, but also improves utilization of the electroactive material due to the avoidance of polymer binder and conducting additives. It is worth mentioning that the unique structure also holds the electrode integration and hence relieves the aggregation and mechanical failure of the active materials after repeated charge/discharge process.[23] Besides, the unique network-like porous nanoarchitectures assembled with ultrathin mesoporous nanosheets of the electroactive ZnO, together with the micropores of the Ni foam substrate, a hierarchical porous electrodes ensure ZnO in high contact with electrolyte and facilitate fast transportation of lithium ions and electrons into the electrode, resulting in an excellent electrochemical performance.[47] In addition, the nickel foam increases the electrical conductivity, avoids the structural deformation, and buffers the large volume change during lithium insertion and extraction process.[48] Benefiting from those advantages, the nickel foam supported network-like ZnO nanoarchitectures with enhanced lithium storage performances are expected to be a promising anodes candidate for high-performance LIBs.

Conclusions

In summary, nickel foam supported network-like ZnO nanoarchitectures assembled with ultrathin mesoporous nanosheets have been fabricated successfully via a facile one-step hydrothermal route. The as-prepared ZnO nanoarchitectures firmly attached to the skeleton of nickel foam, exhibiting network-like porous structures assembled by massive interconnected ultrathin ZnO nanosheets of ~300nm in lateral sizes. Benefiting from the unique network-like mesoporous microstructure and the integrated smart architecture, the ZnO@NF composites exhibit enhanced lithium storage performance as binder-free LIBs anodes. The resultant ZnO@NF electrodes possess a high reversible capacity of 760.5 mAh g^{-1} at a current density of 200 mA g^{-1}, enhanced cycling performance with the capacity maintaining at 534.3 mAh g^{-1} after 100 cycles, and better rate capability compared with the binder-containing counterparts. These results indicate the superiority of the ZnO@NF composites, thus holding great promise for use as high-performance anodes for LIBs.

Acknowledgements

This work was supported by the National Natural Science Foundation of China (Grant No. 51271012).

References

1 M. Armand and J.M. Tarascon, *Nature*, 2008, **451**, 652.
2 B. Dunn, H. Kamath and J. M. Tarascon, *Science*, 2011, **334**, 928.
3 J. Liu, *Adv. Funct. Mater.*, 2013, **23**, 924.
4 N. S. Choi, Z. H. Chen, S. A. Freunberger, X. L. Ji, Y. K. Sun, K. Amine, G. Yushin, L. F. Nazar, J. Cho and P. G. Bruce, *Angew. Chem. Int. Ed.*, 2012, **51**, 9994.
5 R. Marom, S. F. Amalraj, N. Leifer, D. Jacob and D. Aurbach, *J. Mater. Chem.*, 2011, **21**, 9938.
6 W. Y. Li, L. N. Xu and J. Chen, *Adv. Funt. Mater.*, 2005, **15**, 851.
7 Y. G. Li, B. Tan and Y. Y. Wu, *Nano lett.*, 2008, **8**, 265.
8 X. Y. Zhao, M. H. Cao and C. W. Hu, *RSC Adv.*, 2012,**2**, 11737
9 X. J. Zhu, Y. W. Zhu, S. Murali, M. D. Stoller and R. S. Ruoff, *ACS Nano*, 2011, **5**, 3333.
10 S. Q. Ci, J. P. Zou, G. S. Zeng, Q. Peng, S. L. Luo and Z. H. Wen, *RSC Adv.*, 2012, **2**, 5185.
11 M. P. Yu, A. J. Wang, Y. S. Wang, C. Li and G. Q. Shi, *Nanoscale*, 2014, **6**, 11419.
12 Z. W. Fu, F. Huang, Y. Zhang, Y. Chu and Q. Z. Qin, *J. Electrochem. Soc.*, 2003, **150**, A714.
13 X. H. Huang, X. H. Xi, Y. F. Yuan and F. Zhou, *Electrochim. Acta*,

2011, **56**, 4960.
14 V. Cauda, D. Pugliese, N. Garino, A. Sacco, S. Bianco, F. Bella, A. Lamberti and Claudio Gerbaldi, *Energy*, 2014, **65**, 639.
15 X. Y. Shen, D. B. Mu, S. Chen, B. R. Wu and F. Wu, *ACS Appl. Mater. Interfaces*, 2013, **5**, 3118.
16 S. J. Yang, S. Nam, T. Kim, J. H. Im, H. Jung, J. H. Kang, S. Wi, B. Park and C. R. Park, *J. Am. Chem. Soc.*, 2013, **135**, 7394.
17 J. P. Liu, Y. Y. Li, R. M. Ding, J. Jiang, Y. Y. Hu, X. Y. Ji, Q. B. Chi, Z. H. Zhu and X. T. Huang, *J. Phys. Chem. C*, 2009, **113**, 5336.
18 Q. M. Pan, L. M. Qin, J. Liu and H. B. Wang, *Electrochim. Acta*, 2010, **55**, 5780.
19 C. Q. Zhang, J. P. Tu, Y. F. Yuan, X. H. Huang, X. T. Chen and F. Mao, *J. Electrochem. Soc.*, 2007, **154**, A65.
20 Z. Wu, L. M. Qin and Q. M. Pan, *J. Alloys Compd.*, 2011, **509**, 9207.
21 H. B. Wang, Q. M. Pan, Y. X. Cheng, J. W. Zhao and G. P. Yin, *Electrochim. Acta*, 2009, **54**, 2851.
22 L. Xiao, D. D. Mei, M. L. Cao, D. Y. Qu and B. H. Deng, *J. Alloys Compd.*, 2015, **627**, 455.
23 B. Wang, S. M. Li, X. Y. Wu, W. M. Tian, J. H. Liu and M. Yu, *J. Mater. Chem. A*, 2015.
24 L. F. Shen, J. Wang, G. Y. Xu, H. S. Li, H. Dou and X. G. Zhang, *Adv. Energy Mater.*, 2015, **5**, 1400977.
25 C. G. Yang, D. W. Zhang, Y. B. Zhao, Y. H. Lu, L. Wang and J. B. Goodenough, *J. Power Sources*, 2011, **196**, 10673.
26 X. H. Huang, J. P. Tu, X. H. Xia, X. L. Wang and J.Y. Xiang, *Electrochem. Commun.*, 2008, **10**, 1288.
27 M. Kundu, C. C. Albert Ng, D. Y. Petrovykh and L. F. Liu, *Chem. Commun.*, 2013, **49**, 8459.
28 X. H. Huang, R. Q. Guo, J. B. Wu and P. Zhang, *Mater. Lett.*, 2014, **122**, 82.
29 Y. S. Lin and J. G. Duh, *J. Power Sources*, 2011, **196**, 10698.
30 H. G. Jung, S. W. Oh, J. Ce, N. Jayaprakash and Y. K. Sun, *Electrochem. Commun.*, 2009, **11**, 756.
31 H. Kim and J. Cho, *Nano Lett.*, 2008, 8, 3688.
32 Y. G. Li, B. Tan and Y. Y. Wu, *Nano Lett.*, 2008, **8**, 265.
33 H. Liu, G. X. Wang, J. Liu, S. Z. Qiao and H. Ahn, *J. Mater. Chem.*, 2011, **21**, 3046.
34 H. Chen, L. Hu, Y. Yan, R. Che, M. Chen and L. Wu, *Adv. Energy Mater.*, 2013, **3**, 1636.
35 J. Liu, Y. Li, X. Huang, G. Li and Z. Li, *Adv. Funct. Mater.*, 2008, **18**, 1448.
36 J. Wu, C. H. Chen, Y. Hao and C. L. Wang, *Colloids Surf. A*, 2015, **468**, 17.
37 J. F. Li, S. L. Xiong, X. W. Li and Y. T. Qian, *Nanoscale*, 2013, **5**, 2045.
38 D. Zhao, Y. Xiao, X. Wang, Q. Gao and M. H. Cao, *Nano Energy*, 2014, **7**, 124.
39 Z. S. Wu, W. Ren, L. Wen, L. Gao, J. Zhao, Z. Chen, G. Zhou, F. Li and H. M. Cheng, *ACS Nano*, 2010, **4**, 3187.
40 P. Poizot, S. Laruelle, S. Grugeon, L. Dupont and J. M. Tarascon, *Nature*, 2000, **407**, 496.
41 X. H. Huang, R. Q. Guo, J. B. Wu and P. Zhang, *Mater. Lett.*, 2014, **122**, 82.
42 D. Aurbach, *J. Power Sources*, 2000, **89**, 206.
43 G.Y. Huang, S.M. Xu, S.S. Lu, L.Y. Li and H.Y. Sun, *Electrochim. Acta*, 2014, **135**, 420.
44 B. Wang, S.M. Li, J.H. Liu, M. Yu, B. Li, X.Y. Wu, *Electrochim. Acta*, 2014, **146**, 679.
45 Y. Cui, X. L. Zhao and R. S. Guo, *Electrochim. Acta*, 2010, **55**, 922.
46 G. C. Huang, T. Chen, Z. Wang, K. Chang and W. X. Chen, *J. Power Sources*, 2013, **235**, 122.
47 X. H. Huang, J. P. Tu, Z. Y. Zeng, J. Y. Xiang and X. B. Zhao, *J. Electrochem. Soc.*, 2008, **155**, A438.
48 M. Yoshio, T. Tsumura and N. Dimov, *J. Power Sources*, 2005, **146**, 10.

Graphical Abstract

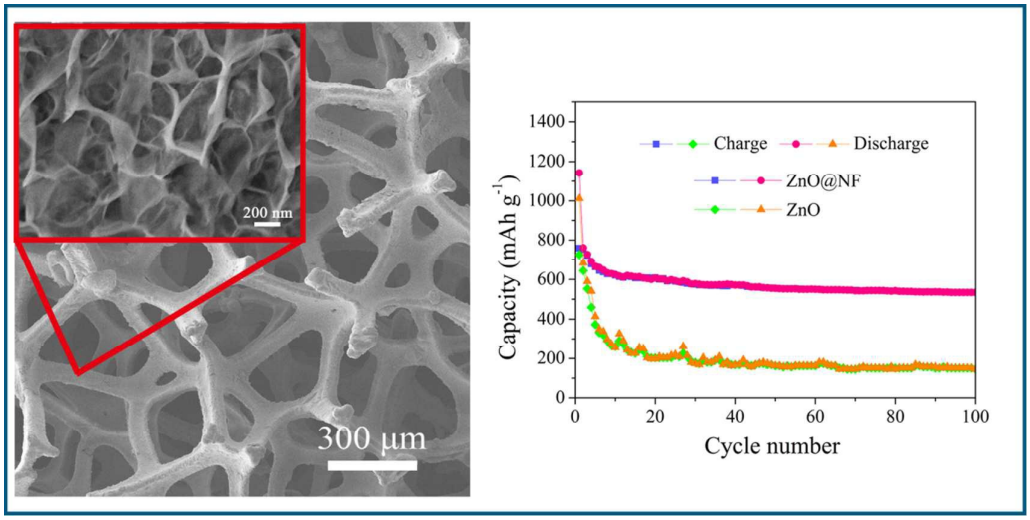

Novel network-like ZnO nanoarchitectures are supported on nickel foam as binder-free anodes for high-performance lithium-ion batteries.